THE ASTROPHYSICAL JOURNAL, 471:774–782, 1996 November 10

THE MACHO PROJECT: LIMITS ON PLANETARY MASS DARK MATTER IN THE GALACTIC HALO FROM GRAVITATIONAL MICROLENSING

C. ALCOCK,[1,2] R. A. ALLSMAN,[3] D. ALVES,[1,4] T. S. AXELROD,[5] A. C. BECKER,[6] D. P. BENNETT,[1,2]
K. H. COOK,[1,2] K. C. FREEMAN,[5] K. GRIEST,[2,7] J. GUERN,[2,7] M. J. LEHNER,[2,7]
S. L. MARSHALL,[1,2] B. A. PETERSON,[5] M. R. PRATT,[2,6,8] P. J. QUINN,[5]
A. W. RODGERS,[5] C. W. STUBBS,[2,5,6,8] AND W. SUTHERLAND[9]
(THE MACHO COLLABORATION)
Received 1996 April 29; accepted 1996 June 13

ABSTRACT

The MACHO project has been monitoring about 10 million stars in the Large Magellanic Cloud (LMC) in the search for gravitational microlensing events caused by massive compact halo objects (MACHOs) in the halo of the Milky Way. In our standard analysis, we have searched this data set for well-sampled, long-duration microlensing light curves, detected several microlensing events consistent with MACHOs in the $0.1\ M_\odot \lesssim m \lesssim 1.0\ M_\odot$ mass range, and set limits on the abundance of objects with masses $10^{-5}\ M_\odot \lesssim m \lesssim 10^{-1}\ M_\odot$. In this paper, we present a different type of analysis involving the search for very short timescale brightenings of stars, which is used to set strong limits on the abundance of lower mass MACHOs. Our analysis of the first 2 years of data toward the LMC indicates that MACHOs with masses in the range $2.5 \times 10^{-7}\ M_\odot < m < 5.2 \times 10^{-4}\ M_\odot$ cannot make up the entire mass of a standard spherical dark halo. Combining these results with those from the standard analysis, we find that the halo dark matter cannot be comprised of objects with masses $2.5 \times 10^{-7}\ M_\odot < m < 8.1 \times 10^{-2}\ M_\odot$.

Subject headings: dark matter — Galaxy: halo — Galaxy: stellar content — gravitational lensing — stars: low-mass, brown dwarfs

1. INTRODUCTION

If a significant fraction of the dark halo of the Milky Way is made up of massive compact halo objects (MACHOs), it should be possible to detect them by searching for gravitational microlensing (Paczyński 1986; Petrou 1981). As a MACHO passes near the line of sight to a background star, the star appears to be magnified by a factor

$$A = \frac{u^2 + 2}{u\sqrt{u^2 + 4}}, \tag{1}$$

where $u = b/r_E$, b is the distance from the MACHO to the line of sight, and the Einstein ring radius r_E is given by

$$r_E = \sqrt{\frac{4GmLx(1-x)}{c^2}}, \tag{2}$$

where m is the mass of the MACHO, L is the observer-star distance, and x is the ratio of the observer-lens and observer-star distances.

Since MACHOs are in motion ($v \sim v_\odot = 220$ km s^{-1}) relative to the line of sight, this magnification is time dependent, with $A(t) = A[u(t)]$, where

$$u(t) = \left\{u_{\min}^2 + \left[\frac{2(t - t_0)}{\hat{t}}\right]^2\right\}^{1/2}. \tag{3}$$

Here t_0 is the time of peak magnification, $u_{\min} = u(t_0)$, and $\hat{t}$ is the event duration, which can be written

$$\hat{t} = 2r_E/v_\perp \sim 130\sqrt{m/M_\odot}\ \text{days}, \tag{4}$$

where $v_\perp$ is the MACHO velocity relative to the line of sight. For more detailed information, see Paczyński (1986) and Griest (1991).

If the halo consisted entirely of objects with masses under about $10^{-4}\ M_\odot$, the average duration of microlensing would be less than 1.5 days, and the events would last only about 3 hr if the halo were made of $10^{-6}\ M_\odot$ objects. In order to clearly see the shape of the microlensing curve for such low-mass lenses, images of a lensed star must be taken in rapid succession during the event. Such an experiment was undertaken by the EROS collaboration (Aubourg et al. 1995), in which a total of about 82,000 stars were imaged up to 46 times per night for several months. No microlensing events were found, and it was reported that objects with masses $5 \times 10^{-8}\ M_\odot < m < 5 \times 10^{-4}\ M_\odot$ cannot comprise the entire Galactic halo at the 90% confidence level (c.l.). We have not followed this approach, but we have used a different technique that is also capable of setting limits on low-mass MACHOs.

The MACHO collaboration has been monitoring the brightnesses of several million stars in the LMC, SMC, and Galactic bulge since 1992 July using the 50 inch (1.27 m) telescope at Mount Stromlo, Australia. A dichroic beam splitter and filters are used to provide simultaneous measurements in red and blue passbands (Alcock et al. 1996b).

[1] Lawrence Livermore National Laboratory, Livermore, CA 94550; alcock, alves, bennett, kcook, stuart@igpp.llnl.gov.
[2] Center for Particle Astrophysics, University of California, Berkeley, CA 94720.
[3] Supercomputing Facility, Australian National University, Canberra, ACT 0200, Australia; robyn@macho.anu.edu.au.
[4] Department of Physics, University of California, Davis, CA 95616.
[5] Mount Stromlo and Siding Spring Observatories, Australian National University, Weston, ACT 2611, Australia; tsa, kcf, peterson, pjq, alex@merlin.anu.edu.au.
[6] Departments of Astronomy and Physics, University of Washington, Seattle, WA 98195; becker, mrp, stubbs@astro.washington.edu.
[7] Department of Physics, University of California, San Diego, CA 92093; kgriest, jguern, mlehner@ucsd.edu.
[8] Department of Physics, University of California, Santa Barbara, CA 93106.
[9] Department of Physics, University of Oxford, Oxford OX1 3RH, UK; w.sutherland@physics.ox.ac.uk.

The observing strategy for the first 2 years of the LMC data was designed to be sensitive to objects with masses $m > 10^{-3}\ M_{\odot}$, so a typical LMC field was generally imaged at most once or twice per clear night. Therefore, microlensing events with durations under a few days will have very few magnified points on their light curves and would show up in our data as upward excursions of one, two, or three consecutive measurements, occurring on stars that otherwise appeared completely normal. In this paper, we search specifically for such short-duration "spike" events. Clearly, if any spikes are detected, no conclusion could be drawn regarding their origin since there would be insufficient detail in the light curves. Therefore, the technique described here is most useful when few if any spikes are found, in which case useful upper limits can be placed on the prevalence of low-mass MACHOs. After applying the selection criteria described below, we do not find any such spikes and so are able to strongly constrain the existence of low-mass objects in the halo of the Milky Way.

2. EVENT SELECTION AND DETECTION

The analysis reported here uses the first 2 years of the LMC data (Alcock et al. 1995a, 1996a, 1996b). Twenty-two fields of 0.5 square degrees each were monitored on every clear night from 1992 July 20 to 1994 October 26, for a total of 10827 observations. A total of about 8.5 million stars are used in this analysis. The images are taken with a refurbished telescope system (Hart et al. 1996) and a special-purpose camera system (Stubbs et al. 1993; Marshall et al. 1994), photometrically reduced using a special-purpose code named SoDoPHOT (Bennett et al. 1996), and assembled into a time series for analysis. Each light curve consists of many measurements of the flux of a star in two filter bands (called "red" and "blue"), as well as estimated errors in the flux measurement and several quantities used to detect probable systematic error in the measurement. These quantities include the crowding, χ^2 of the point-spread function fit, the missing pixel fraction, the cosmic-ray flag, and the sky background. As in the standard analysis, these measures are used to remove suspect data before any further analysis is performed.

Also, as in the standard analysis, several properties of the expected microlensing signal are used to eliminate stars and events that are unlikely to arise from microlensing. After imposing such selection criteria, it is necessary to calculate the number of actual microlensing events that would have been removed by these cuts, and this detection efficiency calculation is discussed in the following sections.

Because this search is for short-duration events, one of the most powerful signatures of microlensing, the shape of the light curve (eqs. [1] and [3]), cannot be used as a selection criterion. Since there are three free parameters for the microlensing light-curve shape, we would need four or more observations during the event to get a meaningful fit. Therefore, any phenomenon that causes a significant upward excursion in one or two observations could be mistaken for very short duration microlensing. Looking through our data, we find many one-observation excursions. A partial list of causes includes satellite tracks and glints, telescope slips, and asteroids. In order to reduce this background, we consider only those instances where two or three exposures were taken of the same star on the same night. Since each exposure gives both red and blue flux measurements, we define a "quad" as a sequence of two (or three) exposures of a star that are on the same night. In the first 2 years of the LMC data, we have 1.44×10^8 quads with two measurements on the same night and 5.8×10^6 quads with three. We then require that all the measurements in the quad be significantly magnified, and we also make use of the fact that, for very short duration microlensing, the measurements of the star on the previous and following nights should not have significant upward excursions. Thus, each quad represents a potential detection of short-duration microlensing events, and because the microlensing rate is proportional to $m^{-1/2}$ (Griest 1991), a substantial number of quads would be magnified if the Milky Way halo were made of low-mass MACHOs.

We define the magnification of a given measurement as

$$A = f/\bar{f}\,, \tag{5}$$

where f is the flux of the measurement and $\bar{f}$ is the median flux of all the points in the relevant passband that pass the quality cuts described above. In order to reduce the statistical probability of random fluctuations in measured flux giving false triggers, we require that all four (or all six) measurements have positive excursions of more than 4 σ, where σ is set by the flux measurement error. That is, we require that the magnification be above a threshold magnification A_T, with $A_T - 1 = 4\,\sigma_{\max}$, where $\sigma_{\max}$ is the largest magnification error of the four or six quad measurements. By using only these sets of measurements and setting a threshold proportional to the error, the probability of a false event detection can be greatly reduced while still allowing a strong limit to be set. With a threshold $A_T - 1 = 4\,\sigma_{\max}$ and a total of 1.5×10^8 quads, the expected number of false triggers from statistical fluctuations is $(3.2 \times 10^{-5})^4 \times 1.5 \times 10^8 = 1.6 \times 10^{-10}$. (This estimate assumes Gaussian errors, so, realistically, the non-Gaussian tails will increase this number substantially.) The 4 $\sigma_{\max}$ threshold was chosen a priori because, after an investigation of several possible analysis methods on a small subset of the data, it appeared most likely to give few (if any) events and to have significant detection efficiency.

In addition to the above criteria, we demand that there be a reasonable number of high-quality data points on the star in order to accurately determine the baseline flux. Thus, we cut on the number of simultaneous red and blue data points and on the average photometric error. In our data set, we have found a large number of periodic and nonperiodic variables that can be eliminated due to the fact that they vary continually, so we also demand that the lensed star not be flagged as a variable. Next, since microlensing is so rare, we do not expect more than one microlensing event to take place on a given star, so we can also eliminate stars in which two or more such events are found. Finally, since gravitational lensing should magnify all wave bands by the same amount, we can demand that the four or six spike points be achromatic within errors. Therefore, we make the following set of cuts:

1. The star must have at least six observations in which both the red and the blue data points pass the cuts in crowding, seeing, etc.
2. The star must have $V - R < 0.9$.
3. Both the red and the blue points in the measurements in the quad, immediately before the quad, and immediately after the quad must pass the cuts in crowding, seeing, etc., and have a magnification error less than 0.5.

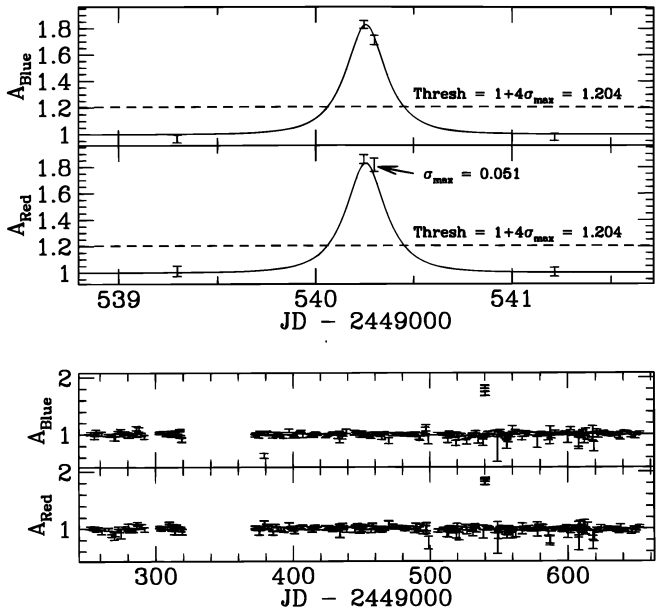

FIG. 1.—A typical Monte Carlo event that passes the cuts used in this analysis. The top two curves are an expanded view of the quad in which the event occurred. Note that the points in the quad are above the threshold of 1.204, and the previous and following measurements are below it. The solid line is the theoretical microlensing curve added to the data. The entire year 2 light curves for the same event are on the bottom. The magnified quad points are clearly visible at day 540.

4. The "robust" χ^2 (that is, a χ^2 fitted with the highest and lowest 10% of the data excluded) of a fit to a constant flux must be less than 0.9 in both red and blue.

5. $A - 1 > 4\,\sigma_{\max}$ for all points in the quad, where $\sigma_{\max}$ is the maximum error of the measurements in the quad.

6. $A - 1 < 4\,\sigma_{\max}$ for the red and blue points in the measurement previous to the quad and the measurement following the quad.

7. The measurements in the quad must be achromatic within errors, that is, $\Delta < 2\,\sigma_\Delta$, where $\Delta = |A_r/A_b - 1|$.

8. There may be at most one event per star.

Cuts 1, 2, 4, and 8 are for the elimination of false events caused by variable stars, cuts 1 and 3 are to eliminate background caused by poor photometry, cut 5 is to reduce the chance of statistical fluctuations or single-observation glitches causing an event, and cut 6 is to eliminate longer duration events. See Figure 1 for an example of our data and a Monte Carlo event that passes these cuts.

These cuts were run on the first 2 years of the LMC data, and no events were found. To test the robustness of these cuts, the analysis was run with thresholds varying between 3 $\sigma_{\max}$ and 5 $\sigma_{\max}$. While a few events were found at thresholds below 4 $\sigma_{\max}$, none were found at the a priori threshold of 4 $\sigma_{\max}$. This will be discussed further in § 6.

3. THEORETICAL EVENT RATES

In order to use our nondetection of spike events to make a statement about the content of the Milky Way halo, we need to predict the number of events we would have expected to find if the halo were made of low-mass MACHOs. Thus, we need to know the efficiency with which our experiment, in combination with the above selection criteria, would have detected short-duration microlensing events if in fact such events occurred. The search for spike events is sensitive to durations of only about 0.1–4 days, corresponding to masses of about 10^{-6} to $10^{-3}\ M_\odot$ (see eq. [4]), and we need to use a halo model to make a connection between event duration, rate, and MACHO mass.

We first consider a simple spherical halo model with mass density

$$\rho(r) = \rho_0 \frac{R_0^2 + a^2}{r^2 + a^2}\,, \tag{6}$$

where $\rho_0 = 0.008\ M_\odot\ \mathrm{pc}^{-3}$ is the local dark matter mass density, r is the distance to the center of the Galaxy, $R_0 = 8.5$ kpc is the distance of the Sun from the Galactic center, and $a = 5$ kpc is the Galactic core radius. Griest (1991) showed that the microlensing rate of a δ-function mass distribution is given by

$$\Gamma = 1.60 \times 10^{-6} u_T / \sqrt{m/M_\odot}\ \text{events yr}^{-1}\,, \tag{7}$$

where $u_T = u(A_T)$, and A_T is the magnification threshold for an event. (The expression for Γ is slightly different from that given in Griest 1991 because we use 50 kpc for the distance to the LMC, rather than 55 kpc.) In an experiment, the number of microlensing events that are expected to be detected is given by

$$N_{\exp} = \Gamma E \mathscr{E}\,, \tag{8}$$

where Γ is the microlensing rate (in event/year/star), E is the effective exposure (in star years), and $\mathscr{E}$ is the average detection efficiency.

The probability of an event occurring with duration $\hat{t}_{\min} < \hat{t} < \hat{t}_{\max}$ can be written

$$P = \frac{1}{\Gamma} \int_{\hat{t}_{\min}}^{\hat{t}_{\max}} \frac{d\Gamma}{d\hat{t}}\, d\hat{t}\,, \tag{9}$$

where, in the approximation of a stationary line of sight, the distribution of event durations is given by (Alcock et al. 1996b)

$$\frac{d\Gamma}{d\hat{t}} = \frac{32 u_T L \rho_0}{m v_0^2 \hat{t}^4} \int_0^1 dx\, \frac{r_E^4(x) A e^{-Q}}{A + Bx + x^2}\,, \tag{10}$$

where $A = (R_0^2 + a^2)/L^2$, $B = -2r_0 \cos b \cos l/L$, b and l are the Galactic coordinates of the source star, $v_0 = 220$ km s^{-1} is the solar circular velocity, and $Q = 4r_E^2(x)/(v_0^2 \hat{t}^2)$. The probability that such an event is actually observed depends strongly on the duration, since the spike selection criteria above eliminate the possibility of detecting long-duration events or events that last only an hour. We can thus define the average efficiency of observing such events as

$$\mathscr{E} = \frac{1}{\Gamma} \int_{\hat{t}_{\min}}^{\hat{t}_{\max}} \frac{d\Gamma}{d\hat{t}}\, \epsilon(\hat{t})\, d\hat{t}\,, \tag{11}$$

where $\epsilon(\hat{t})$ is the detection efficiency as a function of event duration.

4. FINITE-SOURCE EFFECTS

When the impact parameter of the lens is comparable to the size of the lensed object, the magnification can differ significantly from the point-source approximation given in equation (1). For a lensed star with radius R_*, we define

$$U_* = \frac{R_* x}{r_E(x)} \tag{12}$$

as the "effective radius" of the star (the radius of the star normalized to the Einstein radius and scaled to the lens plane). The point-source approximation will then break down completely for $u \lesssim U_*$ because only the fraction of the surface of the star inside the Einstein ring radius will be significantly magnified. In the case of a star of constant surface brightness, we use (Witt & Mao 1994)

$$A = \frac{2}{\pi U_*} + \frac{1 + U_*^2}{U_*^2}\left(\frac{\pi}{2} + \arcsin\frac{U_*^2 - 1}{U_*^2 + 1}\right) \qquad (13)$$

for $u = U_*$, and

$$A = \frac{2(u - U_*)^2}{\pi U_*^2 (u + U_*)} \frac{1 + U_*^2}{\sqrt{4 + (u - U_*)^2}} \Pi\left(\frac{\pi}{2}, n, k\right) + \frac{u + U_*}{2\pi U_*^2}\sqrt{4 + (u - U_*)^2} E\left(\frac{\pi}{2}, k\right) - \frac{u - U_*}{2\pi U_*^2}\frac{8 + (u^2 - U_*^2)}{\sqrt{4 + (u - U_*)^2}} F\left(\frac{\pi}{2}, k\right) \qquad (14)$$

for $u \neq U_*$, where

$$n = \frac{4uU_*}{(u + U_*)^2},$$

$$k = \sqrt{\frac{4n}{4 + (u - U_*)^2}},$$

and F, E, and Π are elliptic integrals of the first, second, and third kind.

There are two effects from the finite-source size. First, the maximum possible magnification,

$$A_{\max} = \frac{\sqrt{4 + U_*^2}}{U_*}, \qquad (15)$$

becomes very low for lower mass lenses. For a star with $R = 10\ R_\odot$ and a lens at $x = 0.5$, we have $A_{\max} = 18.3$ for a lens with $m = 10^{-4}\ M_\odot$. However, with $m = 10^{-6}\ M_\odot$, we have $A_{\max} = 2.08$, and with $m = 10^{-7}\ M_\odot$, we get $A_{\max} = 1.15$. Because we are searching for significant magnifications, this effect would tend to lower the detection efficiency for lower mass lenses. The second effect of a finite-source size is that the star is magnified for a longer period of time. This occurs because a fraction of the star can be close enough to the lens to be significantly magnified, even if the lens is far from the center of the star (see Fig. 2). This effect increases the detection efficiency for low-mass lenses whose average event duration is shorter than the minimum-detectable point-source event timescale. These two effects cancel each other out mostly, with the detection efficiency increasing slightly for very low mass MACHOs.

It is clear that the shape of the light curve is strongly dependent on the lens distance x, so the detection efficiency is a function of both x and $\hat{t}$. Since $\hat{t}$ is a function of both x and $v_\perp$, we use $\epsilon = \epsilon(x, v_\perp)$ in order to simplify the efficiency analysis. The average detection efficiency (eq. [11]) then becomes

$$\mathscr{E} = \frac{1}{\Gamma}\int_0^1 dx \int_0^{v_{\max}} dv_\perp \frac{d\Gamma}{dx\, dv_\perp}\epsilon(x, v_\perp), \qquad (16)$$

where $v_{\max}$ is some upper limit on the perpendicular velocity of the lens. The differential rate used in equation (16) can be

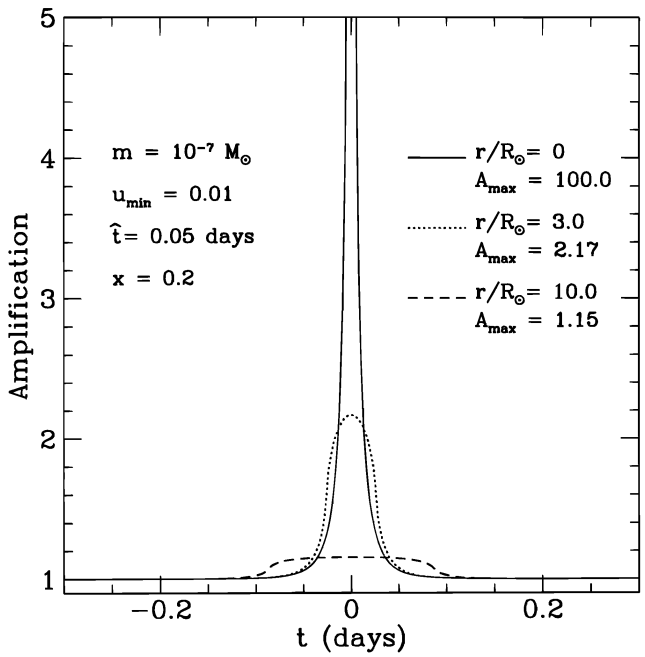

FIG. 2.—A plot of light curves for various source radii. For larger sources, the maximum magnification decreases, but the width of the curve increases.

derived from equation (10) using a simple change of variables:

$$\frac{d\Gamma}{dx\, dv_\perp} = \frac{2u_T L\rho_0 v_\perp^3 \hat{t}}{mv_0^2}\frac{Ae^{-v_\perp^2/v_0^2}}{A + Bx + x^2}. \qquad (17)$$

5. MONTE CARLO AND DETECTION EFFICIENCY

To measure the detection efficiency $\epsilon(x, v_\perp)$, a Monte Carlo simulation was performed in which randomly generated microlensing events were added to each star in the database. Then the same analysis used to search for spike events was performed on these simulated data sets. As a function of the lens position and perpendicular velocity of these events, one can then find the fraction of simulated events that were recovered and define this as $\epsilon(x, v_\perp)$. From simple geometry, one expects microlensing events to have a uniform distribution in minimum impact parameter $u_{\min}$. A minimum error of $0.014A$ is added to each data point, so the minimum 3 $\sigma_{\max}$ threshold is given by $A_T = 1.042$, or $u_{\min} = 2.262$. (As stated previously, the analysis was run on several thresholds varying between 3 $\sigma_{\max}$ and 5 $\sigma_{\max}$, so the minimum threshold was used to set the upper limit of the $u_{\min}$ distribution. This somewhat lowers the detection efficiency for higher thresholds, but the differential microlensing rate given in eq. [17] is correspondingly higher due to the factor of u_T, and there is no net effect in the final result.) Therefore, in performing the Monte Carlo simulation, the simulated microlensing events were added with a uniform distribution of $u_{\min}$ from 0 to 2.262. To adequately sample the widest possible range of event durations and finite-source light-curve shapes, the events were generated using a distribution of x that was uniform over $0 < x < 1$, and a $v_\perp$ distribution uniform over $0 < v_\perp < v_{\max} = 667$ km s^{-1}. In order to improve statistics, the simulated events were forced to peak during a quad (that is, t_0 between the time of measurements previous to and following a quad). The total exposure time used to calculate $N_{\exp}$

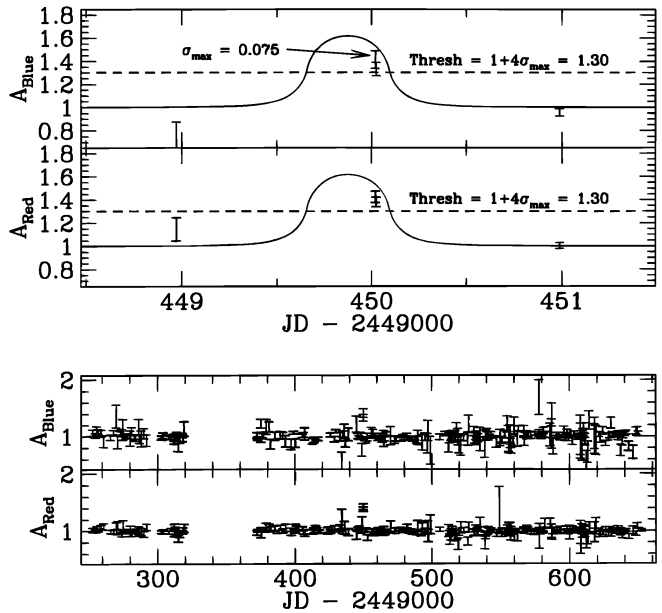

FIG. 3.—A Monte Carlo event with significant blending and finite-source effects. The shape of the theoretical light curve differs from a simple point-source light curve, and the magnified points are below the added magnification because only a fraction of the object is lensed. The event still passes the cuts, and the magnified quad can be seen at day 450 on the entire year 2 light curve.

was adjusted accordingly by using the total "quad time" rather than the length of the observing run. Thus, no simulated events were added during the weeks when the telescope was down.

The shape of the light curve is a function of the radius of the star for low-mass MACHOs, and the radius of a star is correlated with its magnitude. Because brighter stars tend to give lower errors in measured magnification, it follows that the shape of a light curve is correlated with the event-detection threshold. Therefore, the radius of the source was estimated from its color and magnitude, and this radius was used in conjunction with the observer-lens distance x to determine the shape of the simulated light curves. Although limb darkening can change the shape of the light curve (Witt & Mao 1994), limb-darkening coefficients are not well known for such a large sample of stars. An investigation into the effect of limb darkening has shown that the resulting uncertainties in magnification are much smaller than those caused by the uncertainty in the radius of the source star, so the effects of limb darkening are ignored in this analysis.

Since the detection threshold is proportional to the maximum error of the points in a quad, it is important to treat the errors correctly when adding a fake microlensing event to a light curve. The error of the magnification A can be approximated by

$$\sigma = [\sigma_s^2 + (0.014f/\bar{f})^2 + f/\bar{f}^2]^{1/2}\,, \tag{18}$$

where σ_s is the error from sky background, f is the total measured flux of the star, and $0.014f/\bar{f}$ is the minimum error added after photometric analysis. The minimum error is also added in the standard analysis photometry (Alcock et al. 1993, 1995b, 1996b), in order to account for several sources of systematic error in the photometry. There are two limiting cases of the above formula: "sky-dominated" error and "flux-dominated" error. In the case where the error comes mostly from the sky subtraction, the error in the flux does not change significantly when flux is added to create a simulated microlensing event. On the other hand, when the error is dominated by the Poisson statistics of the flux, the error in the added flux should be scaled by $(f)^{1/2}$. Because the flux error is larger, giving higher thresholds, this case was used in the Monte Carlo simulation to get a conservative measure of the efficiency. (The minimum error was subtracted before the errors were adjusted and then added in again afterward, just as the minimum error is added in after the photometric reductions in the standard analysis.) The true efficiency is expected to be closer to the flux error case, because, in general, the sky error contributes significantly only to dim stars that already have a fairly low efficiency due to their large error bars (large threshold).

Because of our crowded fields and poor seeing, many of our photometric objects are actually blends of two or more stars. When a blended star is lensed, the measured magnification can be significantly smaller than the true magnification. To quantify this effect, artificial stars were added to real images taken under a variety of observing conditions, and the photometry code was run again. We thus created a series of response functions of recovered versus added flux, and when a simulated microlensing event is generated, the photometric object is matched to one of these response functions using the object's magnitude. The observing conditions on each point in the light curve are then matched to similar conditions in the response function, and the recovered flux is added to the data. A detailed description of this analysis can be found in Alcock et al. (1996b).

The effects of blending on the detection efficiency are twofold. First, the lower measured magnification will lower the efficiency as fewer quads will be above the threshold magnification. However, if an object is a blend of two or more stars, then there are two or more stars that may be lensed. Thus, the total number of stars in the data set is larger than the number of photometric objects, and our total exposure is increased significantly. A Monte Carlo event with a large blend fraction (and significant finite-source effects) can be seen in Figure 3.

6. RESULTS

Because the blending effects described above are a function of the magnitude of the lensed object, it follows that the detection efficiency depends on the magnitude of the source as well as the lens position and velocity. Using an infinitesimal bin width, the efficiency $\epsilon(x, v_\perp, M)$ can be written

$$\epsilon = \frac{dN_{\rm rec}/dx\,dv_\perp\,dM}{dN_{\rm add}/dx\,dv_\perp\,dM}\,, \tag{19}$$

where M is the average of the red and blue magnitudes of the lensed star (this value is the unblended stellar magnitude that is determined by the blending response function), $N_{\rm add}$ is the number of fake events added to the data, and $N_{\rm rec}$ is the number of these events recovered by the analysis. To calculate the number of expected events, one must integrate the efficiency over the stellar luminosity function $n(M)$:

$$N_{\rm exp} = \int dM \int_0^1 dx \int_0^{v_{\rm max}} dv_\perp \frac{d\Gamma}{dx\,dv_\perp}\,\epsilon(x, v_\perp, M)n(M)T\,, \tag{20}$$

where T is the effective exposure, or "quad time," of a given star. To calculate the efficiency, we have

$$\frac{dN_{\rm rec}}{dx\,dv_\perp\,dM} = \sum_i \delta(x - x_i)\delta(v_\perp - v_{\perp i})\delta(M - M_i)\,, \quad (21)$$

where the sum is over all recovered events. Because we add one simulated event to each object in the database, we can write

$$\frac{dN_{\rm add}}{dM} = n_{\rm sod}(M)\,, \quad (22)$$

where $n_{\rm sod}(M)$ is the SoDoPHOT object luminosity function (that is, the luminosity distribution of objects recovered by the photometric reductions of the images). This function is used because the response function stellar magnitudes follow the SoDoPHOT object distribution and the response functions are chosen uniformly from this distribution (Alcock et al. 1996b). The events are added uniformly in x and $v_\perp$, which gives

$$\begin{aligned}\frac{dN_{\rm add}}{dx\,dv_\perp\,dM} &= \frac{d^2}{dx\,dv_\perp}\,n_{\rm sod}(M)\,,\\ &= \text{const}\;n_{\rm sod}(M)\,,\\ &= \frac{n_{\rm sod}(M)}{v_{\rm max}}\,, \end{aligned} \quad (23)$$

where the factor $1/v_{\rm max}$ is a normalization constant. The number of expected events then becomes

$$N_{\rm exp} = \sum_i \frac{d\Gamma}{dx\,dv_\perp}\bigg|_{x_i, v_{\perp i}} \frac{n(M_i)}{n_{\rm sod}(M_i)}\,T_i\,v_{\rm max}\,. \quad (24)$$

Approximately 6.5% of the stars used in this analysis can be found in more than one field (Alcock et al. 1996b), and we must scale the number of expected events accordingly. However, the possibility of double counting in this analysis occurs only when double or triple exposures are taken on overlapping fields on the same night. This only happens in about $\frac{2}{3}$ of our quads, so we subtract 4.4% from our number of expected events rather than 6.5%.

A plot of $N_{\rm exp}$ versus mass for a δ-function mass distribution is given in Figure 4. At the peak at $10^{-5}\,M_\odot$, about 17 events would be expected to have been found if the halo is as modeled in equation (6) and consisted entirely of MACHOs of that mass. Equivalently, we may convert the number of expected events into upper limits on the allowed halo mass fraction that can be contributed from objects in the excluded mass range. Such a plot is given in Figure 5. Using the fact that no events were found, we can place strong limits on the halo of the Milky Way. When $N_{\rm obs} = 0$, the Poisson 95% c.l. upper limit is $N_{\rm exp} = 3$ events, so for the simple spherical halo model, masses between $2.5 \times 10^{-7}\,M_\odot$ and $5.2 \times 10^{-4}\,M_\odot$ are ruled out at the 95% c.l. Although these limits are for a δ-function mass distribution, any model distribution containing a combination of masses in this range is also ruled out at the 95% c.l. (Griest 1991; Alcock et al. 1996b).

Figures 4 and 5 also show the results from the EROS CCD experiment (Aubourg et al. 1995). Although they give a stronger limit for $m < 10^{-6}\,M_\odot$, the limits set by this analysis give the strongest limits to date for $10^{-6}\,M_\odot \lesssim m \lesssim 10^{-3}\,M_\odot$.

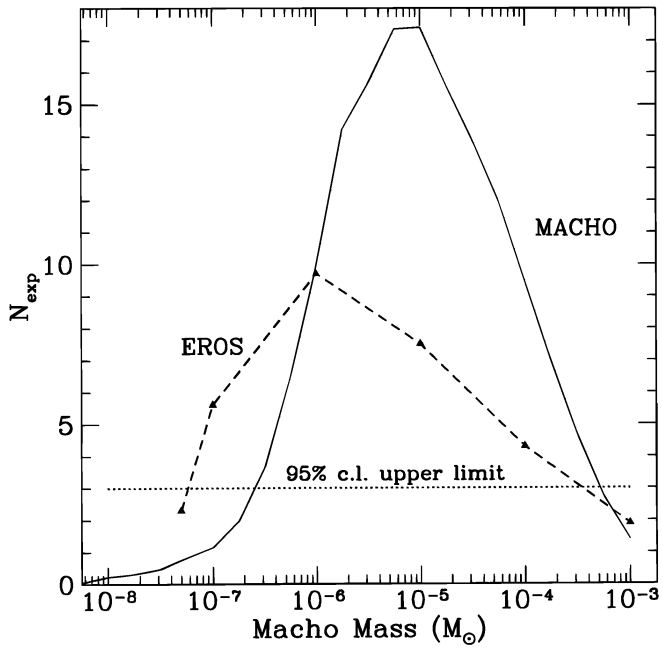

FIG. 4.—A plot of the number of expected events vs. mass for a δ-function mass distribution. With no events found, the 95% c.l. upper limit is three events, and the region of the curve above this limit is excluded. The number of expected events from the EROS CCD experiment is also shown.

As mentioned previously, the analysis was run with thresholds varying from 3 $\sigma_{\rm max}$ to 5 $\sigma_{\rm max}$ in order to determine the robustness of the analysis. A plot of the number of expected and observed events as a function of threshold can be found in Figure 6, and the corresponding plot of halo fraction upper limit versus threshold can be found in Figure 7. A total of 11 events were found that passed various thresholds between 3 $\sigma_{\rm max}$ and 3.75 $\sigma_{\rm max}$, but no events were

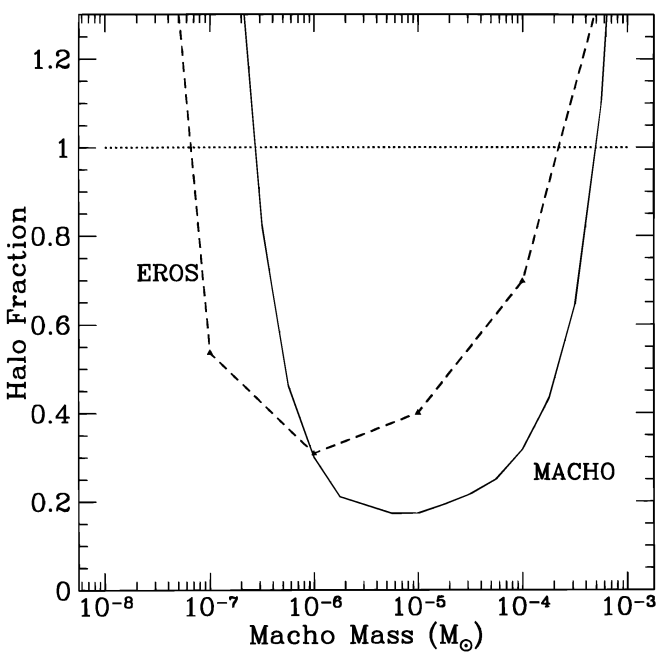

FIG. 5.—A plot of allowed halo mass fraction vs. mass for a δ-function mass distribution. The region above the solid line is excluded at the 95% c.l. The halo fraction upper limit from the EROS CCD experiment is also shown.

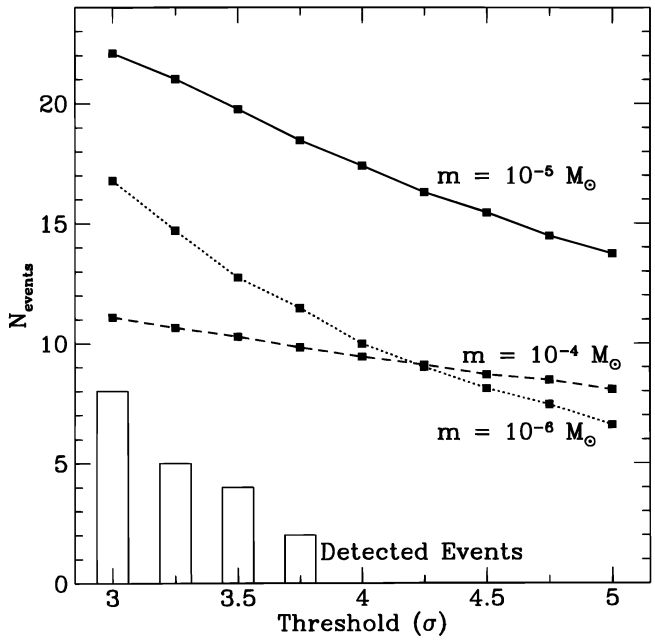

FIG. 6.—Number of expected events as a function of threshold for three values of MACHO mass. The number of observed events as a function of threshold are also shown.

found at thresholds of 4 σ_{max} and higher. Of the 11 events found, eight were on stars with $V < 17.5$ and are likely low-level variables that fell through the variable star cuts. Of the three remaining events, two occurred in the same field on the same night, which indicates possible problems with the observations, and inspection of the second image in the quad shows a likely telescope slip during the exposure. The remaining event passes only the 3 σ_{max} threshold cut. In order to reduce these backgrounds in future analysis runs, stars with $V < 17.5$ will be cut, as will images with more than one event. It has been determined that these cuts will reduce the number of expected events by about 20%. However, because neither the number of expected events nor the number of observed events varies drastically with threshold, the analysis using the a priori 4 σ_{max} threshold is robust, and the limits set on the abundance of low-mass MACHOs are valid.

7. COMBINED ANALYSES

The standard analysis method of fitting microlensing curves to the data is sensitive to MACHOs of masses 10^{-5} $M_\odot < m < 1$ $M_\odot$, and it would be useful to combine the results of the two types of analyses. To avoid double counting of events that could pass both the spike and the standard cuts, we ran the standard analysis cuts on any simulated events passing the spike event cuts, and any events passing both sets of cuts are so flagged. The efficiency is then recalculated with the flagged events considered as failing the cuts, and the number of expected events can then be added to the number of expected events from the standard analysis. However, when adding the number of expected events, the number of observed events must also be added. The standard analysis of the first 2 years of the LMC data yields eight likely microlensing events (Alcock et al. 1996a) that would make the combined limit on halo fraction very weak. However, the eight events all have durations $\hat{t} > 34$ days, and it is very unlikely that these events were caused by MACHOs with $m < 0.1$ $M_\odot$. Therefore, the standard analysis efficiency was recalculated with a cut such that the event duration must be shorter than 20 days. (20 days was chosen in order to be conservative.) The number of expected events thus drops significantly at $m > 0.1$ $M_\odot$, but we also have no observed events and are able to place strong limits on lower mass objects. The number of expected events and halo fraction versus lens mass can be found in Figures 8 and 9. Here it can be seen that MACHOs of masses 2.5×10^{-7} $M_\odot < m < 8.1 \times 10^{-2}$ $M_\odot$ cannot

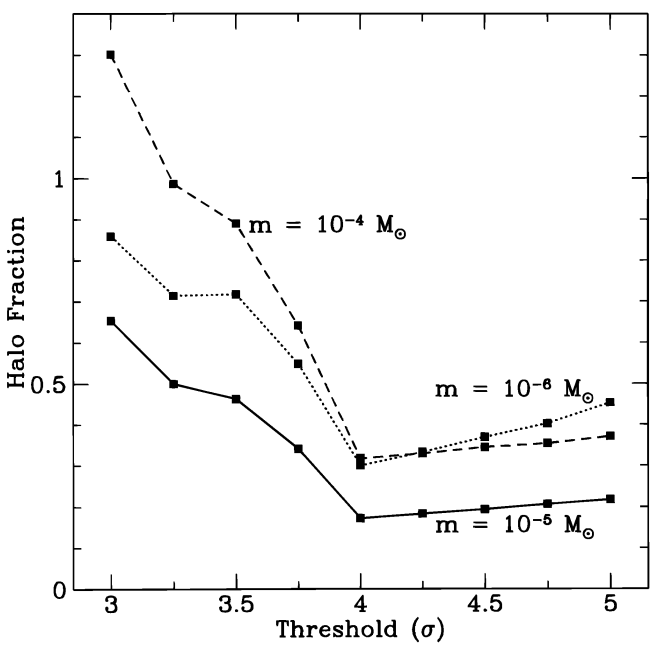

FIG. 7.—Halo fraction upper limit (95% c.l.) as a function of threshold for three values of lens mass. The upper limit rises at lower thresholds because events are detected at these thresholds, and the 95% c.l. upper limit on N_{exp} increases accordingly.

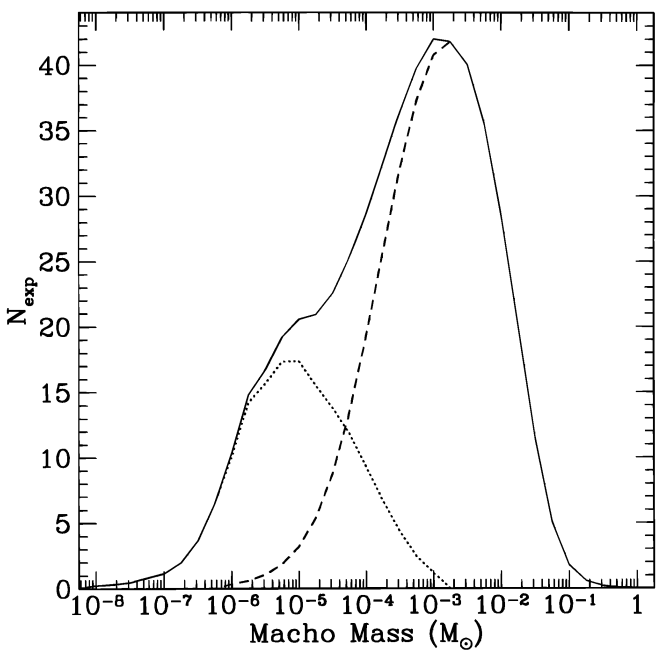

FIG. 8.—Number of expected events as a function of MACHO mass after combining the standard and spike analyses, with a cut on events with $\hat{t} > 20$ days. The spike result is plotted with the dotted line (with the double-counted events subtracted), the standard result with the dashed line, and the combined result is shown with the solid line.

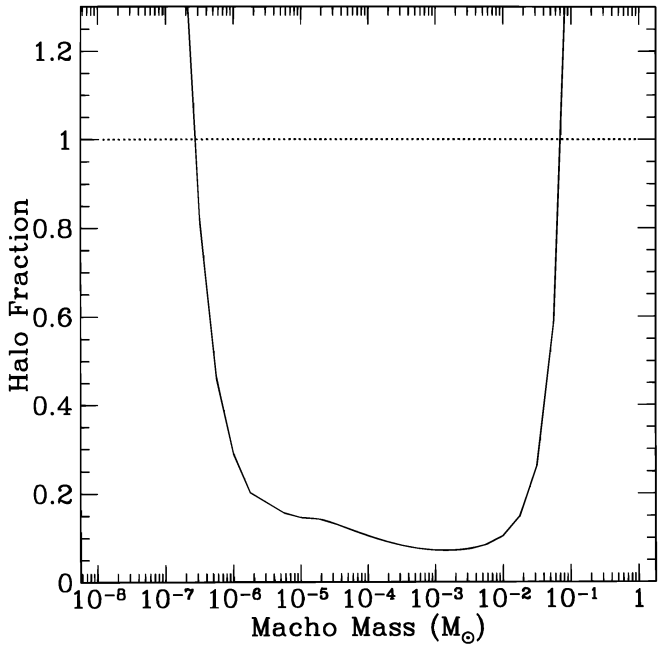

FIG. 9.—Halo fraction upper limit (95% c.l.) for the combined spike and standard analyses and with $\hat{t} < 20$ days.

make up the entire halo mass, and lenses in the range $1.88 \times 10^{-6}\ M_\odot < m < 2.5 \times 10^{-2}\ M_\odot$ comprise at most 20% of the halo dark matter.

8. POWER-LAW HALO MODELS

The halo models of N. W. Evans (Evans 1994; Evans & Jijina 1994) allow for rising or falling rotation curves, flattened halos, and various disk contributions to the total Galactic mass. These models are also called "power-law" models because, at large Galactic radii R, the circular velocity $v_{\rm circ} \propto R^{-\beta}$ for some model parameter β. The parameters used to describe the mass and velocity distributions in these models are as follows:

1. β: at large Galactic radii, $\beta = 0$ gives a flat rotation curve, $\beta < 0$ gives rising curve, and $\beta > 0$ gives falling curve.
2. q: halo flattening parameter; $q = 1$ gives spherical halo, $q = 0.7$ represents ellipticity of E6.
3. v_0: normalization velocity.
4. R_c: Galactic core radius. A large R_c gives a massive disk.
5. R_0: radius of solar orbit.

The differential event rate $d\Gamma/dx\,dv_\perp$ can be derived as a function of these parameters (Alcock et al. 1995c), and it is then straightforward to calculate the number of expected events using equation (24). Limits were calculated for the same models used in Alcock et al. (1996b), and the parameters used are found in Table 1. For each model, Table 1 shows the total mass inside 50 kpc from the center of the Milky Way, which we call M_{50}.

Model S is the simple standard spherical halo described in § 3, and model A is the power-law model equivalent. Model B has a rising rotation curve and a more massive halo, while model C has a falling curve and a less massive halo. Model D has a flattened halo, and models E, F, and G have more massive disks. Model E has an extremely massive disk and a very light halo, and this model is probably inconsistent with estimates of the mass of the Milky Way.

TABLE 1

POWER-LAW HALO MODEL PARAMETERS

Model	β	q	v_0 (km s^{-1})	R_c (kpc)	R_0 (kpc)	M_{50} ($10^{11}\ M_\odot$)
S	...	...	...	5	8.5	4.13
A	0	1	200	5	8.5	4.62
B	−0.2	1	200	5	8.5	7.34
C	0.2	1	180	5	8.5	2.36
D	0	0.71	200	5	8.5	3.74
E	0	1	90	20	7.0	0.82
F	0	1	150	25	7.9	2.10
G	0	1	180	20	7.9	3.26

The number of expected events was calculated for these models and then combined with the results from the standard analysis as described in § 7. In Figure 10, we plot the resulting number of expected events as a function of lens mass for a δ-function mass distribution using the simple spherical halo model and the seven power-law halo models described above. Figure 11 is a plot of allowed halo fraction versus mass for the same models. For the models with more massive halos, only about 30% of the halo can be comprised of MACHOs in the range of $9.5 \times 10^{-7}\ M_\odot < m < 2.9 \times 10^{-2}\ M_\odot$. The limits get weaker for less massive halos, and little useful parameter space can be excluded for the extreme "maximal disk" model E.

The differences between the limits among the various models is primarily because the number of expected events is directly proportional to M_{50}, or the number of MACHOs in the halo. We can get more model-independent limits by removing this factor and plotting the total allowed halo mass from MACHOs inside 50 kpc, rather than the halo mass fraction, as a function of mass. This plot is shown in

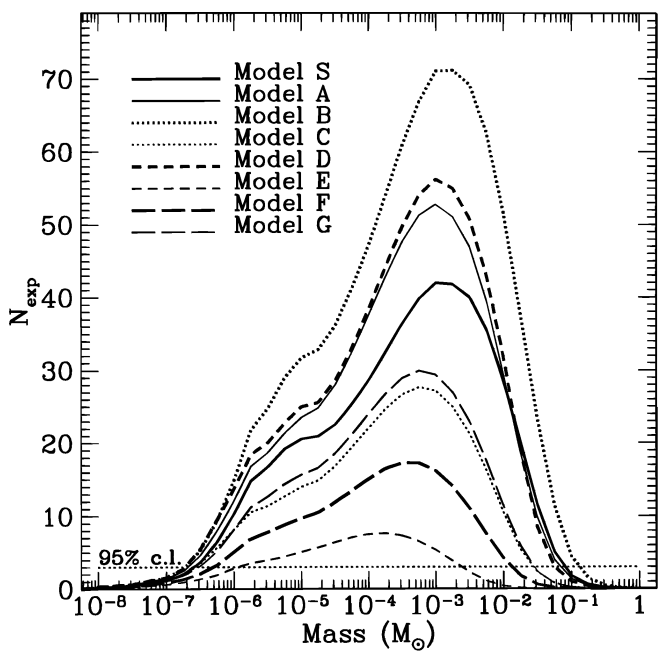

FIG. 10.—A plot of the number of expected events vs. mass for the standard model and seven power-law halo models. The results shown are for the combined spike and standard analyses, and with $\hat{t} < 20$ days. The line at $N_{\rm exp} = 3$ is the 95% c.l. upper limit, and the regions of the curves above this line are ruled out.

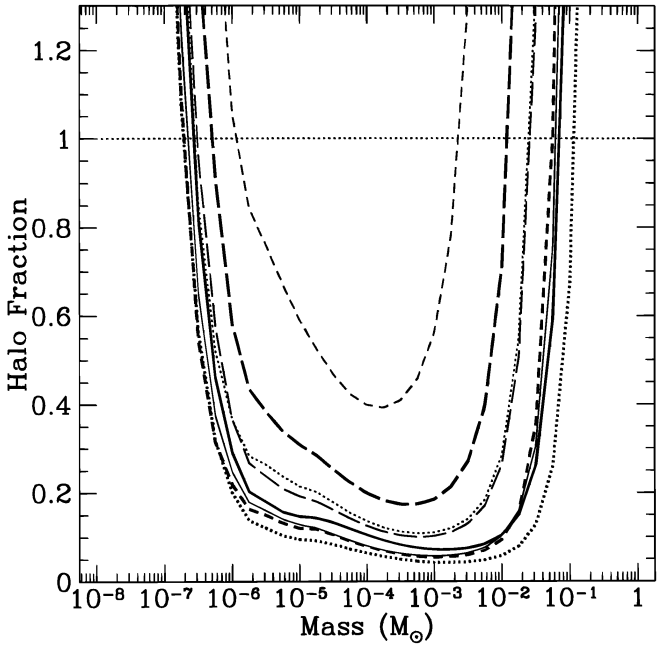

FIG. 11.—Upper limits on MACHO fraction of the halo vs. lens mass for the spherical and power-law halo models (line coding is the same as in Fig. 10). The results shown are for the combined spike and standard analyses, and with $\hat{t} < 20$ days. The regions above the curves are ruled out at the 95% c.l.

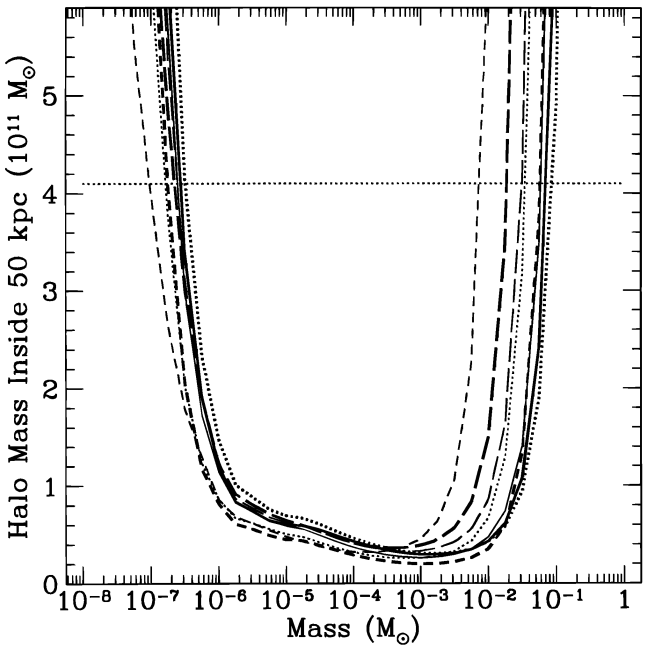

FIG. 12.—Upper limits on the total mass of MACHOs interior to 50 kpc as a function of lens mass. The results shown are for the combined spike and standard analyses, and with $\hat{t} < 20$ days. The regions above the curves are ruled out at the 95% c.l. Objects of mass $3.2 \times 10^{-7}\ M_\odot < m < 1.87 \times 10^{-2}\ M_\odot$ cannot make up the canonical value of $4.1 \times 10^{11}\ M_\odot$, independent of the model used.

Figure 12. Ignoring the unlikely model E, we see that, independent of model, no more than $10^{11}\ M_\odot$ of the halo mass inside 50 kpc can come from objects of mass $1.85 \times 10^{-6}\ M_\odot < m < 6.5 \times 10^{-3}\ M_\odot$, and objects in the range $3.2 \times 10^{-7}\ M_\odot < m < 1.87 \times 10^{-2}\ M_\odot$ cannot make up the entire canonical value of $4.1 \times 10^{11}\ M_\odot$.

9. CONCLUSION

We have extended the sensitivity of the MACHO experiment to 2 orders of magnitude lower in mass by using existing data and without changing observing strategy. Objects with masses $2.5 \times 10^{-7}\ M_\odot < m < 8.1 \times 10^{-2}\ M_\odot$ (roughly one Mars mass to 80 Jupiter masses) cannot comprise the entire standard spherical halo mass, and MACHOs in the range $1.88 \times 10^{-6}\ M_\odot < m < 2.5 \times 10^{-2}\ M_\odot$ make up less than 20% of the halo. Independent of halo model, objects in the range of $3.2 \times 10^{-7}\ M_\odot < m < 1.87 \times 10^{-2}\ M_\odot$ cannot make up the canonical halo mass inside 50 kpc of $4.1 \times 10^{11}\ M_\odot$, and less than $10^{11}\ M_\odot$ of the halo is made from MACHOs with masses $1.85 \times 10^{-6}\ M_\odot < m < 6.5 \times 10^{-3}\ M_\odot$. These limits are the strongest published to date. We also plan to run this analysis on the data from the Galactic bulge, which may allow us to place strong limits on the abundance of low-mass MACHOs in the disk and bulge of the Milky Way.

We are grateful for the support given our project by the technical staff at the Mount Stromlo Observatory. Work performed at LLNL is supported by the DOE under contract W-7405-ENG-48. Work performed by the Center for Particle Astrophysics personnel is supported by the NSF through AST 91-20005. The work at MSSSO is supported by the Australian Department of Industry, Science, and Technology. K. G. acknowledges support from DOE OJI, Alfred P. Sloan, and Cotrell Scholar awards. C. S. acknowledges the generous support of the Packard and Sloan Foundations. W. S. is supported by a PPARC Advanced fellowship. M. L. thanks Thor Vandehei for assistance in running the analysis.

REFERENCES

Alcock, C., et al. 1993, Nature, 365, 621
———. 1995a, Phys. Rev. Lett., 74, 2867
———. 1995b, ApJ, 445, 133
———. 1995c, ApJ, 449, 28
———. 1996a, ApJ, in press
———. 1996b, ApJ, 461, 84
Aubourg, E., et al. 1995, A&A, 301, 1
Bennett, D., et al. 1996, in preparation
Evans, N. W. 1994, MNRAS, 267, 333
Evans, N. W., & Jijina, J. 1994, MNRAS, 267, L21
Griest, K. 1991, ApJ, 366, 412
Hart, J., et al. 1996, PASP, 108, 220
Marshall, S., et al. 1994, in IAU Symp. 161, Astronomy from Wide Field Imaging, ed. H. T. MacGillivray et al. (Dordrecht: Kluwer), 67
Paczyński, B. 1986, ApJ, 304, 1
Petrou, M. 1981, Ph.D. thesis, Cambridge Univ.
Stubbs, C. W., et al. 1993, Proc. SPIE, 1900, 192
Witt, H. J., & Mao, S. 1994, ApJ, 430, 505